Anisotropic wind in massive system REX-1: a new window onto critical rotation and gamma-ray bursts

J. R. Callingham,[1,2*] P. G. Tuthill,[2] B. J. S. Pope,[2,3,4] P. M. Williams[5],
P. A. Crowther,[6] M. Edwards,[2] B. Norris,[2] and L. Kedziora-Chudczer[7]

[1]ASTRON, Netherlands Institute for Radio Astronomy,
PostBus 2, 7990 AA, Dwingeloo, The Netherlands
[2]Sydney Institute for Astronomy (SIfA), School of Physics,
The University of Sydney, NSW 2006, Australia
[3]Center for Cosmology and Particle Physics, Department of Physics,
New York University, 726 Broadway, New York, NY 10003, USA
[4]NASA Sagan Fellow
[5]Institute for Astronomy, University of Edinburgh,
Royal Observatory, Edinburgh EH9 3HJ, UK
[6]Department of Physics & Astronomy, University of Sheffield,
Sheffield, S3 7RH, UK
[7]School of Physics, University of New South Wales,
NSW 2052, Australia
[*]To whom correspondence should be addressed; E-mail: callingham@astron.nl

One sentence summary: New high-mass star system exhibits anisotropic mass loss, indicating a supernova precursor system with near-critical rotation.

The massive evolved Wolf-Rayet stars sometimes occur in colliding-wind binary systems in which dust plumes are formed as a result of the collision of stellar winds. These structures are known to encode the parameters of the binary orbit and winds. Here we report observations of a new Wolf-Rayet system, REX-1, with a spectroscopically determined wind speed of

$\approx 3400 \; \mathrm{km\,s^{-1}}$. In the thermal infrared, REX-1 is adorned with a prominent $\approx 12''$ spiral dust plume, revealed by proper motion studies to be expanding at only $\approx 430 \, \mathrm{km\,s^{-1}}$: nearly an order of magnitude slower. As the dust and gas appear coeval, these observations are inconsistent with existing models of the dynamics of such colliding wind systems. We propose this contradiction can be resolved if the system is capable of launching extremely anisotropic winds. Physical processes capable of driving such a wind imply that REX-1 could constitute a unique local laboratory: an analog to long-duration gamma-ray burst progenitors.

Late-type carbon-rich WR (WC) stars with binary companions have the potential to produce spiral "Pinwheel" patterns in which dust forms at the interface between the colliding stellar winds (1,2). As the orbital motion entangles the winds, the form of the plume encodes the primary wind and orbital parameters, forming rare and powerful laboratories for testing our understanding of the mass-loss in WR stars. For well studied Pinwheels such as WR 104 (2,3), WR 98a (4) and WR 140 (3), nearly complete solutions can be obtained that tightly constrain the windspeeds, momentum ratio, orbital parameters and system distance. For such systems, the dust (studied by its proper motion in the thermal infrared) and the gas (the dominant wind component revealed by spectroscopy) have been shown to be comoving (5). This immediately yields a model-independent geometric distance, fixing all parameters of the binary wind system in absolute units. WR stars play a significant role in the chemistry and kinetic energy budget of the interstellar medium (5), and are considered to be likely progenitors to long-duration gamma-ray bursts (6–8) and, ultimately, LIGO black-hole binary systems (9). Understanding WR mass-loss and angular momentum evolution is therefore critical to informing our understanding of some of the most energetic events and environments in the universe.

2

REX-1 (RA: 16:00:50.48, Dec: -51:42:45.4; epoch J2000) was first noted as a high luminosity outlier in our Galactic plane X-ray and radio survey, and revealed as a truly exceptional object on crossmatching its infrared spectral energy distribution (SED) (10), where it brightens from an apparent magnitude of 6.4 at $2.2\,\mu$m to -2.4 at $22\,\mu$m (11). Such dramatic brightening to the far infrared is indicative of luminous objects embedded within an extremely dusty environment. To explore the morphology of the dust nebula, and so divine the nature of the source, we observed REX-1 with the mid-infrared camera VISIR (12) on the European Southern Observatory's (ESO) Very Large Telescope (VLT) on 13 August 2016. The spectacular dust plume revealed at $8.9\,\mu$m is shown in Figure 1, exhibiting a form strongly reminiscent of the Archimedean spirals produced by the Wolf-Rayet Pinwheels. Perhaps the closest resemblance is with the more complex forms exhibited by WR 140 (13, 14) rather than prototype system WR 104 (2).

To identify the stellar spectral types and prospect for the presence of the expected fast ($\gtrsim 1000\,\mathrm{km\,s^{-1}}$) wind in the system, we observed REX-1 using the near-infrared NACO camera (15, 16) and integral field spectrometer SINFONI (17), also on the VLT. The $2.24\,\mu m$ NACO observation (Figure 1, inset) resolves REX-1 into a $0.739'' \pm 0.002''$ binary with a fainter companion to the North. When registered against the VISIR images, the brighter southern component (hereafter "the Central Engine") was found to exactly coincide with the mid-infrared peak central to the major structural elements of the dust plume. The Northern companion is just visible as a minor asymmetric feature at the corresponding location in the wings of the mid-infrared core.

Several further lines of evidence imply that the Northern companion is unlikely to play any significant role in sculpting the dust plume. Assuming a distance of 1.8 kpc, the companion is $\approx 1300\,\mathrm{AU}$ from the Central Engine: several orders of magnitude wider than the normal range for Pinwheel binaries (3). The corresponding orbital period of at least

3

10^4 years is entirely unrealistic to wrap winds into a spiral in the manner of a Pinwheel system (required windspeeds are $<< 1\,\mathrm{km\,s^{-1}}$) (3,4). Furthermore, the non-thermal radio emission from our $19.7\,\mathrm{GHz}$ Australia Telescope Compact Array (ATCA) observations of the system also falls entirely on the Central Engine, with no offset to the North.

The SINFONI instrument was able to isolate spectra for both the Central Engine and Northern companion, with the J- and $H+K$-band spectra of the Central Engine presented in Figure 2. The presence of a WR star in the Central Engine is immediately confirmed by the absence of hydrogen lines and the characteristic broad helium and carbon lines (18). The ratio of the C III and C IV lines, and the abnormal strength of the He II lines, suggests the presence of a WR star with a spectral type of WC7 or a WR star in the brief transitory phase between nitrogen and carbon-rich (WN/WC) (19, 20). Both subtypes have winds $\gtrsim 1700\,\mathrm{km\,s^{-1}}$ (5). We spectroscopically measured the windspeed of the Central Engine of REX-1 via the $1.083\,\mu\mathrm{m}$ He I line (21) using the long-slit spectrograph IRIS2 (22) on the $3.9\,\mathrm{m}$ Anglo Australian Telescope (AAT). As shown in Figure 6, a fit to the P-Cygni profile of the $1.083\,\mu\mathrm{m}$ He I line provides a direct spectroscopic measurement that a wind exists in the system with a terminal velocity $v_\infty = 3400 \pm 200\,\mathrm{km\,s^{-1}}$.

Because fast WR winds usually result in proper motions that are readily apparent on short timescales, an additional VISIR epoch was observed on 1 August 2017, approximately one year after the original VISIR image. Confounding expectations, the differential imagery registered a very slow expansion of the plume with structures found to be uniformly inflating at $50 \pm 6\,\mathrm{mas\,yr^{-1}}$ (see Supplementary Section 1.2). At $1.8\,\mathrm{kpc}$ this corresponds to an expansion velocity of $430 \pm 50\,\mathrm{km\,s^{-1}}$ —- nearly an order of magnitude slower than the fast wind measured spectroscopically, and well below lower bounds for any WR wind (5) for which limits can be traced to fundamental escape velocity arguments. The classical prototype Pinwheels exhibit no such discrepancy: angular and spectroscopic

expansion speeds are consistent and simply related by the distance.

Several straightforward arguments might attempt to explain this deep contradiction in the properties of the REX-1 wind. Angular and Doppler speeds would be reconciled if REX-1 were nearly ten times further away than indicated. However, this scenario is ruled out by kinematic distance limits (see Supplementary Section 1.3), and furthermore it would boost intrinsic luminosities by a factor of 100 making REX-1 the brightest persistent X-ray and radio colliding wind-binary (CWB) system in the Galaxy (23) (more luminous by an order of magnitude in radio emission than η Carinae when it is not in outburst (24)). Although it is difficult to conceive of an environment capable of mounting sustained resistance to a WR wind, the idea of some form of wind braking or pressure confinement might be proposed. Apart from the difficulty of finding a mechanism to contain the momentum (by a factor of 10) of the most powerful stellar winds known, the clean form and detailed sharp structure in the dust plume of Figure 1 argue strongly against a confinement argument. The medium performing the braking would have to be highly uniform or else it would disrupt the plume's symmetry, and would likely be susceptible to Rayleigh-Taylor induced instabilities which are not apparent here (25).

Stagnant dust structures have recently been reported in two other WR systems: WR 112 and WR 122. The fragmented shell-like structures seen in WR 112 (26) led the authors to conclude that the structure arose from previous periods of Roche lobe overflow, while the suggestion for WR 122 (27) is a dusty nebula left over from a prior phase of binary mass transfer. While the existing explanations for both these systems invoke a switch in state from a past episode of mass loss governed by different physics, we believe this idea is unlikely to work for REX-1. Unlike these stagnant systems, REX-1 exhibits a precisely constrained expansion speed allowing the entire structure to be kine-matically aged. Dust in the outermost coils of the nebula would have been ejected from

the Central Engine about 125 years previously (see Supplementary Section 1.2), while many of the innermost features are significantly younger ($\leq 50\,\mathrm{yr}$). Under the hypothesis of a recent switch-in-state from slow to fast, the latter wind (now an order of magnitude faster) should rapidly overtake and collide with prior slow-wind structures. The timescale for this is very short —- the fast WR wind should sweep the entire volume of the plume in a little over a decade. One would expect such an event to disrupt the elegantly sculpted slow plume. Therefore to invoke a similar scenario to those proposed for WR112/WR122, we must be witnessing a privileged moment where the switch has occurred very recently (within the last 5 years or so): a highly suspect coincidence.

With the fast and slow winds observationally confirmed (by spectroscopy and proper motion respectively), and with both manifest simultaneously in the REX-1 system, we propose that this duality of the wind must be intrinsic to the system. The most natural scenario in which all the evidence can be made to fit together is one in which the central engine WR is capable of launching both a slow and fast wind. Anisotropic winds, for example configured as a fast polar and slow equatorial flow, have been established in other settings (28, 29) with rapid stellar rotation most often invoked as the underlying driver (30, 31). For the case of REX-1, spectroscopic analysis of the SINFONI data, as well as the presence of the spiral plume, points to the central engine hosting an unresolved CWB, possibly WR-WR or WR-O (see Supplementary Section 1.4). As the orbit of the binary companion takes it through the equatorial plane occupied by the slow heavy wind from the primary, a colliding-wind plume will result by way of the Pinwheel mechanism. Dust may continue to expand at the slow rate inflating the embedded spiral plume structure, unhampered by the fast polar wind with which it will never interact. This neatly ties together all the phenomenology, removing the conflict between spectroscopic and proper motion windspeeds, and implying a CWB orbital period comparable to the $\sim 125\,\mathrm{yr}$ plume

dynamical age.

In the event these lines of evidence pointing to an extreme anisotropic wind driven by rapid rotation in a WR host star are verified, the REX-1 system presents a new, local astrophysical laboratory to study an exotic configuration. Angular momentum evolution through the transition to the Wolf-Rayet phase is poorly understood with varying mechanisms capable of yielding wildly divergent outcomes in rotation (31). Long-duration gamma-ray bursts are thought to originate from the core-collapse supernova of a star with high angular momentum, near its critical rotation rate (32, 33). We would place REX-1 (and potentially also WR 112/WR 122) into a new class of system as a nearby analog to such stars, and further detailed study will test gamma-ray burst models that have previously largely only been confronted with post-explosion data at extragalactic distances.

References

1. P. M. Williams, et al., MNRAS 243, 662 (1990).

2. P. G. Tuthill, J. D. Monnier, W. C. Danchi, Nature 398, 487 (1999).

3. P. G. Tuthill, et al., ApJ 675, 698 (2008).

4. J. D. Monnier, P. G. Tuthill, W. C. Danchi, ApJ 525, L97 (1999).

5. P. A. Crowther, ARA&A 45, 177 (2007).

6. S. E. Woosley, A. Heger, ApJ 637, 914 (2006).

7. R. G. Detmers, N. Langer, P. Podsiadlowski, R. G. Izzard, A&A 484, 831 (2008).

8. A. Levan, et al., Space Sci. Rev. 202, 33 (2016).

9. P. Marchant, N. Langer, P. Podsiadlowski, T. M. Tauris, T. J. Moriya, A&A 588, A50 (2016).

10. M. F. Skrutskie, et al., AJ 131, 1163 (2006).

11. E. L. Wright, et al., AJ 140, 1868 (2010).

12. P. O. Lagage, et al., The Messenger 117, 12 (2004).

13. P. M. Williams, K. A. van der Hucht, H. van der Woerd, W. M. Wamsteker, T. R. Geballe, Instabilities in Luminous Early Type Stars, H. J. G. L. M. Lamers, C. W. H. De Loore, eds. (1987), vol. 136 of Astrophysics and Space Science Library, pp. 221–226.

14. J. D. Monnier, P. G. Tuthill, W. C. Danchi, ApJ 567, L137 (2002).

15. R. Lenzen, et al., Instrument Design and Performance for Optical/Infrared Ground-based Telescopes, M. Iye, A. F. M. Moorwood, eds. (2003), vol. 4841 of Proc. SPIE, pp. 944–952.

16. G. Rousset, et al., Adaptive Optical System Technologies II, P. L. Wizinowich, D. Bonaccini, eds. (2003), vol. 4839 of Proc. SPIE, pp. 140–149.

17. F. Eisenhauer, et al., Instrument Design and Performance for Optical/Infrared Ground-based Telescopes, M. Iye, A. F. M. Moorwood, eds. (2003), vol. 4841 of Proc. SPIE, pp. 1548–1561.

18. L. F. Smith, MNRAS 138, 109 (1968).

19. P. A. Crowther, L. J. Hadfield, J. S. Clark, I. Negueruela, W. D. Vacca, MNRAS 372, 1407 (2006).

20. C. K. Rosslowe, P. A. Crowther, Monthly Notices of the Royal Astronomical Society 473, 2853 (2018).

21. P. R. J. Eenens, P. M. Williams, MNRAS 269, 1082 (1994).

22. C. G. Tinney, et al., Ground-based Instrumentation for Astronomy, A. F. M. Moorwood, M. Iye, eds. (2004), vol. 5492 of Proc. SPIE, pp. 998–1009.

23. A. M. T. Pollock, P. A. Crowther, K. Tehrani, P. S. Broos, L. K. Townsley, MNRAS 474, 3228 (2018).

24. M. De Becker, F. Raucq, A&A 558, A28 (2013).

25. E. R. Parkin, J. M. Pittard, M. G. Hoare, N. J. Wright, J. J. Drake, MNRAS 400, 629 (2009).

26. R. M. Lau, et al., ApJ 835, L31 (2017).

27. J. Mauerhan, et al., MNRAS 450, 2551 (2015).

28. J. H. Groh, D. J. Hillier, A. Damineli, ApJ 638, L33 (2006).

29. J. H. Groh, A. S. Oliveira, J. E. Steiner, A&A 485, 245 (2008).

30. C. Aerts, H. J. G. L. M. Lamers, G. Molenberghs, A&A 418, 639 (2004).

31. T. Shenar, W.-R. Hamann, H. Todt, A&A 562, A118 (2014).

32. S. E. Woosley, ApJ 405, 273 (1993).

33. G. Gräfener, J. S. Vink, T. J. Harries, N. Langer, A&A 547, A83 (2012).

34. F. Pérez, B. E. Granger, Computing in Science and Engineering 9, 21 (2007).

35. E. Jones, T. Oliphant, P. Peterson, Others, SciPy: Open source scientific tools for python (2001).

36. J. D. Hunter, Computing In Science & Engineering 9, 90 (2007).

37. Astropy Collaboration, et al., A&A 558, A33 (2013).

38. S. Van Der Walt, S. C. Colbert, G. Varoquaux, Computing in Science & Engineering 13, 22 (2011).

39. R. I. Davies, MNRAS 375, 1099 (2007).

40. W. E. Wilson, et al., MNRAS 416, 832 (2011).

41. R. J. Sault, P. J. Teuben, M. C. H. Wright, Astronomical Data Analysis Software and Systems IV, R. A. Shaw, H. E. Payne, J. J. E. Hayes, eds. (1995), vol. 77 of Astronomical Society of the Pacific Conference Series, p. 433.

42. J. R. Callingham, S. A. Farrell, B. M. Gaensler, G. F. Lewis, M. J. Middleton, ApJ 757, 169 (2012).

43. K. A. Arnaud, Astronomical Data Analysis Software and Systems V, G. H. Jacoby, J. Barnes, eds. (1996), vol. 101 of Astronomical Society of the Pacific Conference Series, p. 17.

44. G. Zasowski, et al., ApJ 798, 35 (2015).

45. J. C. Mauerhan, S. D. Van Dyk, P. W. Morris, AJ 142, 40 (2011).

46. C. K. Rosslowe, P. A. Crowther, MNRAS 447, 2322 (2015).

47. D. Majaess, Ap&SS 344, 175 (2013).

48. C. M. Dutra, E. Bica, J. Soares, B. Barbuy, A&A 400, 533 (2003).

49. D. Froebrich, A. Scholz, C. L. Raftery, MNRAS 374, 399 (2007).

50. D. Camargo, E. Bica, C. Bonatto, MNRAS 455, 3126 (2016).

51. W. S. Dias, et al., A&A 564, A79 (2014).

52. N. Zacharias, et al., AJ 145, 44 (2013).

53. D. Minniti, et al., New Astronomy 15, 433 (2010).

54. X. Chen, R. de Grijs, L. Deng, MNRAS 464, 1119 (2017).

55. A. Damineli, et al., MNRAS 463, 2653 (2016).

56. Gaia Collaboration, et al., A&A 595, A2 (2016).

57. C. K. Rosslowe, P. A. Crowther, MNRAS 473, 2853 (2018).

58. P. R. J. Eenens, P. M. Williams, R. Wade, MNRAS 252, 300 (1991).

59. M. P. Egan, S. D. Price, AJ 112, 2862 (1996).

60. G. Neugebauer, et al., ApJ 278, L1 (1984).

61. P. A. Crowther, L. J. Smith, A&A 305, 541 (1996).

62. A. Z. Bonanos, et al., ApJ 611, L33 (2004).

63. P. Massey, K. Grove, ApJ 344, 870 (1989).

64. V. Muntean, A. F. J. Moffat, A. N. Chené, A. de La Chevrotière, MNRAS 399, 1977 (2009).

65. A. Sander, W.-R. Hamann, H. Todt, A&A 540, A144 (2012).

66. P. M. Williams, et al., MNRAS 420, 2526 (2012).

67. S. A. Zhekov, et al., MNRAS 445, 1663 (2014).

68. B. Bohannan, P. A. Crowther, ApJ 511, 374 (1999).

69. J. H. Groh, A. Damineli, F. Jablonski, A&A 465, 993 (2007).

70. E. F. Schlafly, et al., ArXiv e-prints (2017).

71. J. E. Drew, et al., MNRAS 440, 2036 (2014).

72. N. Epchtein, et al., A&A 349, 236 (1999).

73. M. F. Skrutskie, et al., AJ 131, 1163 (2006).

74. D. Ishihara, et al., A&A 514, A1 (2010).

75. I. Yamamura, et al., VizieR Online Data Catalog 2298 (2010).

76. S. D. Price, M. P. Egan, S. J. Carey, D. R. Mizuno, T. A. Kuchar, AJ 121, 2819 (2001).

77. S. Molinari, et al., A&A 591, A149 (2016).

78. A. Pauldrach, A. Herrero, A&A 199, 262 (1988).

79. A. Damineli, et al., MNRAS 463, 2653 (2016).

80. P. M. Williams, K. A. van der Hucht, P. S. Thé, A&A 182, 91 (1987).

81. V. G. Zubko, V. Mennella, L. Colangeli, E. Bussoletti, MNRAS 282, 1321 (1996).

82. P. W. Morris, K. R. Brownsberger, P. S. Conti, P. Massey, W. D. Vacca, ApJ 412, 324 (1993).

83. G. E. Anderson, et al., ApJ 727, 105 (2011).

84. S. A. Zhekov, M. Gagné, S. L. Skinner, ApJ 727, L17 (2011).

85. M. G. Watson, et al., A&A 493, 339 (2009).

86. J. D. Monnier, L. J. Greenhill, P. G. Tuthill, W. C. Danchi, ApJ 566, 399 (2002).

87. D. C.-J. Bock, M. I. Large, E. M. Sadler, AJ 117, 1578 (1999).

88. T. Murphy, et al., MNRAS 382, 382 (2007).

89. B. J. Rickett, W. A. Coles, G. Bourgois, A&A 134, 390 (1984).

90. P. Benaglia, et al., A&A 579, A99 (2015).

91. J. Wilms, A. Allen, R. McCray, ApJ 542, 914 (2000).

Acknowledgements

critiqued the manuscript. M. E. and B. N. reduced the VISIR and NACO data. L. K-C. conducted the IRIS2 observation.

Competing interests: The authors have no competing interests with respect to this manuscript.

Data and materials availability: All data included in this manuscript are now available in the public domain. The VISIR, NACO, and SINFONI data are available through the ESO archive. The ATCA data are available through the Australia Telescope Online Archive (ATOA). The IRIS2 data are available through the AAT Data Archive. The X-ray data are available through the XMM-Newton Science Archive (XSA) and Chandra data archive.

1 Supplementary materials

CONTENTS:

Observations and data reduction

Differential image and measuring the proper motion of the dust spiral

Distance and possible open cluster association

Alternative spectral types for the Central Engine

Spectral properties of the distant Northern companion

Optical and infrared photometry of REX-1

X-ray properties of REX-1

Radio properties of REX-1

Figs. 4 to 11

Tables 1 to 4

References (34-91)

1.1 Observations and data reduction

1.1.1 NACO

REX-1 was observed 2016 April 28 with NACO on the VLT in three different filters, $2.24\,\mu$m, $3.74\,\mu$m, and $4.05\,\mu$m. The $3.74\,\mu$m and $4.05\,\mu$m images were taken with the L27 camera with a pixel scale of 27.15 mas/pix, and the $2.24\,\mu$m image was taken with the S13 camera, which has a scale of 13.22 mas/pix. The $4.05\,\mu$m observations were taken using chopping and hardware windowing of the detector, with a chopping frequency of $\approx 0.1\,$Hz. The observations, magnitudes, and angular separation of the Central Engine and Northern companion are summarised in Table 1.

The NACO data were reduced via the standard ESO pipeline (v4.4.3). Dark subtraction, flat fielding, and sky subtraction were performed on the standard star and REX-1. The sky frame for all filters were computed from frames that were taken 5-10 minutes either side of the REX-1 frame. The task `jitter` was used to produce the image data. Zero points for all filters were calculated using the standard star HD 144648. Since two other 2MASS stars were detected in the $2.24\,\mu$m observations, we corrected to the astrometric scale of 2MASS with a shift of $\approx 0.5''$ vertically and $\approx 2''$ horizontally. The resulting K-band image is shown in the inset of Figure 1.

We note that the $2.24\,\mu$m image of the Central Engine shows that the source is slightly resolved. A two-dimensional isotropic Gaussian was fit to the visibilities as function of baseline, finding a best fit of $\sigma = 28 \pm 12$ mas, assuming 2% visibility uncertainty. We do not obtain a satisfactory fit with a binary model. We expect that this measurement is dominated by systematics rather than the 12 mas statistical uncertainty, but it can be safely stated that the central engine is marginally resolved in the NACO images.

1.1.2 VISIR

Mid-Infrared imaging observations were made with the VISIR instrument on 2016 August 13 and 2017 August 1 in the $8.9\,\mu$m filter, as well as on 2016 July 23 in the $11.7\,\mu$m filter. All images had a plate scale of 45mas/pix, and implemented a parallel chop-nod pattern with a chopping frequency of $\approx 4\,$Hz. The 2016 VISIR data was reduced using the chopping and nodding method via the standard ESO developed pipeline (v4.3.1). Due to an incorrect setting in the observing block, the chopping amplitude for the 2017 data was somewhat too small, however the impact of this on the final data products was minor. Full imagery was recovered by judicious application of a window functions, although this required some custom processing codes. The resulting $8.9\,\mu$m of the 2017 August 1 epoch, after applying a high-pass filter, is shown in the left panel of Figure 4.

1.1.3 SINFONI

We observed REX-1 using the near-IR integral field spectrometer SINFONI instrument (17) at the VLT in J- and $H+K$-bands on 2017 July 21. The nominal spectral resolution for SINFONI in J- and $H+K$-band is 2000 and 1500, respectively. REX-1 was observed for a total ≈ 25 minutes in each band, with nodding performed every $30\,$s and $3\,$s for J- and $H+K$-band, respectively. A plate scale of $0.1''\,\mathrm{pixel}^{-1}$ were used for both filters, providing a $3'' \times 3''$ field-of-view. The observations were adaptive-optics assisted using a natural guide star. We observed the standard star HIP 082670 to correct for spectral telluric features.

The standard ESO SINFONI pipeline (v3.0.0) via Gasgano was used to perform the data reduction. Dark subtraction, flat fielding, detector linearity, geometrical distortion, and wavelength calibration were applied to REX-1, the standard star, and sky frames. Sky subtraction was then performed via the standard pipeline (39).

The standard star's spectrum was extracted from a data cube using an aperture three times larger than the PSF to ensure all the flux was captured. The spectrum was then normalised by a black body curve of the appropriate temperature. Intrinsic spectral features of the standard star were removed through modelling of the lines with Lorentzian profiles before correcting for atmospheric transmission curves in the science data cubes.

The resulting science $H+K$-band image is shown in Figure 5, indicating that REX-1 is resolved by SINFONI into two sources. We also summed the J-band data over the Central Engine and Northern companion to derive the J-band magnitudes of 10.2 ± 0.2 and 9.6 ± 0.2, respectively.

1.1.4 IRIS2

On 2017 March 16, we observed REX-1 with the long-slit spectrograph IRIS2 (22) on the 3.9 m AAT at the Siding Spring Observatory, Australia. The IRIS2 instrument is based on a HAWAII1 HgCdTe detector, and can achieve a spectral resolution of $\lambda/\Delta\lambda \approx 2400$, where λ is the observing wavelength. Our observation was conducted using the J_s-filter, which is sensitive between 1.041 and 1.256 μm. Exposure times were 18 s on REX-1 before nodding REX-1 to another position along the slit. A total of eights scans were taken, resulting in a total of 2.5 h on source. HIP 73881 was the standard star observed to correction for atmospheric transmission features, of which ten scans of 18 s length were taken. The IRIS2 slit has a width of 1″ on sky, implying that the long-slit spectrum observed will be a combination of both sources identified in the SINFONI image presented in Figure 5.

The data reduction of J_s-band used the standard routines in the Image Reduction and Analysis Facility (IRAF, v2.16) software. Firstly, the spectra were flat-fielded and dark corrected. Spectra were extracted, as well as sky subtracted, for each scan via the task

apall. Wavelength calibration was done using a Xe arc lamp spectra. Each scan of the standard star was combined using the task scombine, and the Paschen-γ absorption feature $1.094\,\mu$m was removed via fitting a Lorentzian profile. After combining all the science spectra, the telluric features were removed using the task telluric. The total resulting spectra, extracted for the full $1''$ aperture, of REX-1 is shown in Figure 6. To remove the presence of the Northern companion from the $1.083\,\mu$m He I line, the aperture used to extract the spectrum was adjusted to isolate the broad component, which corresponds to emission from the WR star in the Central Engine (21). The line with the contamination of the Northern companion removed is presented in Figure 6.

1.1.5 ATCA

We observed REX-1 on 2017 May 11 with the ATCA in the 6A array configuration, which facilitates the highest resolution imaging of any ATCA configuration. The observations were conducted at the central frequencies of 2.1 and 17/19 GHz, with total integration times of 180 and 200 minutes, respectively. The Compact Array Broadband Backend (CABB; (40)) provides instantaneous 2 GHz bandwidth for both linear polarizations at all frequencies. Each observation used a 10 second correlator integration time and 1 MHz channels. Antenna-1 (CA01) was not available during the observations due to maintenance activities.

The calibrators PKS B0823-500 and PKS B1921-293 were used for flux density and bandpass calibration of the 2.1 and 17/19 GHz observations, respectively. PKS B0823-500 is known to be slightly variable, introducing a 10% systematic uncertainty in the flux density scale in the 2.1 GHz-centred observation. The flat-spectrum source PMN J1534-5351 was the phase calibrator for all frequencies. PMN J1534-5351 was observed after 30 minutes on source for frequencies below 10 GHz. For the 17/19 GHz observations, the

phase calibrator was targeted after 20 minutes on source, and pointing calibration was performed every 50 minutes using PKS B1921-293.

The data was reduced using the miriad software package (41). Initially, we flagged areas of known radio frequency interference (RFI) and lower sensitivity in CABB. Excision of RFI from the flux density and bandpass calibrators was performed using the automatic flagging option in the task `pgflag`, and then manually with `blflag`. For the observation centred on $2.1\,\mathrm{GHz}$, $\approx 30\%$ of the data was flagged. For all the other observations, $\approx 10\%$ of the data was flagged. The instantaneous $2\,\mathrm{GHz}$ bandwidth was split into four $512\,\mathrm{MHz}$ wide subbands, in which bandpass, gain and leakage solutions were estimated using the flux density calibrator and ten second time intervals. The calculated calibration solutions were transferred to the phase calibrator PMN J1534-5351. RFI excision was similarly performed before calculating the phase solutions and ensuring the flux density of PMN J1534-5351 was bootstrapped to the flux density scale defined by the gain calibrator. All calibration solutions were then transferred to REX-1.

We applied multi-frequency synthesis over the $512\,\mathrm{MHz}$ bandwidth of each subband to image REX-1 with a robust parameter of -1.0. The images were cleaned to the first negative clean component before going through a phase self-calibration step using the shallowly cleaned images as a model. After re-imaging the self-calibrated data, the images were cleaned more deeply to approximately three times the theoretical rms level. The resulting rms noise in for the 1.4 and $19.7\,\mathrm{GHz}$ images varied from ≈ 1 to $\approx 8\times 10^{-2}\,\mathrm{mJy\,beam^{-1}}$, respectively. The contours of the $19.7\,\mathrm{GHz}$ image is shown in the inset of Figure 1.

1.1.6 Chandra and XMM-Newton

REX-1 was observed between 0.2 and $10.0\,\mathrm{keV}$ on three separate occasions by the XMM-Newton observatory, and once by the Chandra X-ray observatory. The Chandra X-ray

observatory detection and two of the XMM-Newton observatory detections of REX-1 were recorded serendipitously, since REX-1 is located within $10'$ of the well-studied supernova remnant (SNR) G330.2+1.0. The X-ray observatory, epoch, observatory observation identification numbers, off-axis angle of REX-1 during the observation, and the available X-ray instruments during the observation, are provided in Table 2. The counts of the X-ray observations make REX-1 the fourth brightest CWB thus far detected.

The XMM-Newton data were reduced following the standard procedure (42). The XMM-Newton Science Analysis System (version 16.0.0) software was used to ingest the observation data files and to produce the source spectra. The European Photon Imaging Camera (EPIC) data was filtered for background flares, resulting in the effective exposure times listed in the final column of Table 2.

We selected appropriate spectral extraction regions depending on the off-axis angle of REX-1. Background spectra were extracted from the same CCD as the source spectra with annular areas two times larger than the source extraction region. To minimise the impact of pile-up, only single events were included in the production of the spectra. Photon redistribution matrices and ancillary response files were constructed for the spectra, which were than grouped into 20 counts per energy bin before being read into XSPEC (version 12.9.1; (43)) for model fitting.

The Chandra X-ray observatory observations were reduced using the Chandra Interactive Analysis of Observations (CIAO, version 4.9) software and the calibration database CALDB (version 4.7.5.1). A summary of the Chandra observation is also presented in Table 2. REX-1 was detected with the Advanced CCD Imaging Spectrometer (ACIS)-I3 at a large off-axis angle of $8.6'$. Time-dependent gain correction, the latest map of the ACIS gain, and a correction for charge transfer inefficiency were all applied to the data. The data was filtered for flaring and bad event grades.

For spectroscopy, response and effective area files were produced using the CIAO task specextract. The resulting source and background spectra were also grouped in 20 counts per energy bin and converted into a file format that could be read into XSPEC.

1.2 Differential image and measuring the proper motion of the dust spiral

As noted in the body text, proper motions witnessed over the ~ 1 year interval between the two VISIR epochs were about one order of magnitude smaller than anticipated. Although simple differential imaging did reveal a detectable apparent expansion, extracting quantitative estimates of this small signal required further image processing. Firstly the reduced and cleaned VISIR images from both epochs were highpass filtered with a 20-pixel ($0.9''$) Gaussian kernel, accentuating edges and boundaries of the plume (see Left Panel of Figure 4). The expansion over the elapsed time interval is observed in the differential highpass image shown in the Right Panel of Figure 4. The result is consistent with a uniform isotropic expansion of the astrophysical structures over time, but not with noise processes such as a change in seeing between the intervals.

Although the differential image was highly instructive in a qualitative sense to establish the presence of inflation, the quantitative extraction of the windspeed required further analysis. This was performed by fitting a piecewise linear curve to the ridge crests in the highpass filtered images at each epoch separately. The radial displacements of these data points were then registered against each other over the two epochs, and then averaged over arcs that represented each of the major structural curves that go to making up the filtered images. The edges in the plume were all found to exhibit positive radial displacements between 2016 and 2017, with the range from about 0.7 pixel up to 1.2 pixel, with most of the features (distributed all around the arc) close to the high end of this range. We believe that this range in values most likely represents the fact that not all the edges are moving

exactly in the plane of the sky, resulting in some apparent slowing due to projection.

To get a quantitative estimate of the expansion speed, we took the mean of the four fastest (presumably least projected) features which gave a value of $50 \pm 6\,\mathrm{mas\,yr^{-1}}$. At a distance of $1.8\,\mathrm{kpc}$, this corresponds to an expansion velocity of $430 \pm 50\,\mathrm{km\,s^{1}}$.

Given such a well defined (and seemingly constant) outflow speed everywhere around the plume, we are able to estimate the dynamical age of any feature in dust assuming an origin at the central engine. Most of the outermost spiral features are at about 6.3 arcseconds away, implying an ejection from the core 125 ± 15 years ago.

1.3   Distance and possible open cluster association

Due to the presence of diffuse interstellar bands (DIBs) in the spectra of REX-1, we can place an upper limit on the distance to the system. The detected DIB at $1.527\,\mu\mathrm{m}$ has an equivalent width of $1.02 \pm 0.04\,\text{Å}$. Based on the relationship between the equivalent width of the $1.527\,\mu\mathrm{m}$ DIB line and foreground extinction A_v, this implies the distance to REX-1 is $\lesssim 4.5\,\mathrm{kpc}$ (44).

Since the Central Engine is likely composed of a WC7 + WN3-4 or WN/WC + O (see Section 1.4), we can also use the infrared photometry of REX-1 to estimate the distance to the system (19, 45). If the Central Engine is a WN/WC + O, and provided the WN/WC component is similar to WR26 (46), in J-band (where the dust contribution is minimised) the WN/WC star contributes two-thirds of the light based on the ratio of the He II lines at 1.16 and $1.28\,\mu\mathrm{m}$. Since the entirety of the Central Engine has a J-band flux of 10.2, this implies the extinction in J-band is $A_J \approx 3.5$, providing a distance estimate of $1.8\,\mathrm{kpc}$ (20, 46). If the Central Engine is composed of a WC7 + WN3-4, the absolute magnitudes in the J-band for both stars are -4.2 and -3.7 (46), respectively, providing a distance estimate of $1.9\,\mathrm{kpc}$.

The distance to REX-1 can also be inferred from its possible association with an open cluster. The position of REX-1 is co-incident with the young open cluster Majaess 170, as shown in Figure 7. Majaess 170 was identified via mid-infrared colours from the WISE survey (47). The classification of Majaess 170 as an embedded open cluster had been missed by previous searches using such surveys as 2MASS (e.g. (48, 49)) due to the heavy dust obscuration causing a significant fraction of the cluster's stellar content to be inaccessible at optical and near-infrared wavelengths. Such heavily obscured clusters represent the youngest stellar environments in the Milky Way (50). The cluster membership of Majaess 170 is shown by the red squares in Figure 7 (51), as found using optical proper motions derived from the fourth U.S. Naval Observatory CCD Astrograph Catalog (UCAC4; (52)). Unfortunately, REX-1 was not detected in UCAC4 since its optical magnitude was below the UCAC4 R-band magnitude limit of ≈ 16. A Cepheid member of the cluster was identified via the VISTA Variables in the Vía Láctea (VVV; (53)), providing a distance to Majaess 170 of $1.8 \pm 0.2\,\text{kpc}$ and derived a dust extinction of $E(J - H) = 0.38 \pm 0.03$ (54).

Since the position of REX-1 is less than $\approx 30''$ from the cluster centre, and because the stellar composition of REX-1 is consistent with a heavy star-forming environment such as a young embedded open cluster, it is possible that REX-1 is associated with Majaess 170. Such an association provides a distance to REX-1 of $1.8 \pm 0.2\,\text{kpc}$, which is consistent with the distance derived using infrared photometry.

However, the presence of a WR star in an open cluster with a Cepheid is abnormal since the evolutionary time for a Cepheid to form implies WR stars should not still exist in the cluster (5). Additionally, the A_v derived from the $1.527\,\mu\text{m}$ DIB line suggests a dust extinction of $E(J-H) \sim 1$ (55), higher than that derived for the open cluster. Such a dust extinction implies it is likely REX-1 lies behind Majaess 170 or suffers local reddening,

which would be unsurprising given its dusty nebula and crowded environment (55). The association with Majaess 170 at least provides a lower-limit to the distance to REX-1 of 1.6 kpc.

Therefore, all lines of evidence suggest that REX-1 is located $\lesssim 4.5\,\text{kpc}$, and likely around $d \approx 1.8\,\text{kpc}$. We expect that the geometric distance to REX-1 will be established with great precision in Gaia (56) Data Release 2, which will accordingly allow us to improve our estimate of the absolute fluxes and geometric dust expansion rate.

The X-ray and radio luminosities also suggest the system should not be significantly further away than $1.8\,\text{kpc}$. As alluded to in the main text, if we were to put the system at a distance of $\approx 9\,\text{kpc}$ to make the proper motion velocity of the dust spiral consistent with the spectroscopically measured wind velocity, the 0.2-10 keV X-ray and 1.4 GHz radio luminosity of REX-1 would be $L_{0.2-10\,\text{keV}} \approx 2 \times 10^{35}\,\text{erg s}^{-1}$ and $L_{1.4\,\text{GHz}} \approx 3 \times 10^{31}\,\text{erg s}^{-1}$, respectively. Such luminsoities would make REX-1 the brighest persistent X-ray CWB in the Galaxy (23), and an order of magnitude brighter in radio emission than η Carinae, the brightest radio CWB (for direct comparison to Table A.5 of (24), the radio luminosity of REX-1, integrated over the bandpass of 0.33 to 30 GHz, is $L_{\text{rad}} \approx 2 \times 10^{32}\,\text{erg s}^{-1}$ at this distance).

If we place the system at $4.5\,\text{kpc}$, corresponding to the upper limit derived from the kinematic distance, we still have a factor of over three discrepancy between the velocity of the dust spiral and the spectroscopically measured wind velocity, and luminosities of $L_{0.2-10\,\text{keV}} \approx 5 \times 10^{34}\,\text{erg s}^{-1}$ and $L_{1.4\,\text{GHz}} \approx 6 \times 10^{30}\,\text{erg s}^{-1}$ ($L_{\text{rad}} \approx 5 \times 10^{31}\,\text{erg s}^{-1}$). Such luminosities would make REX-1 the third most luminous CWB in X-rays (23) and with a similar radio luminosity as η Carinae when not in outburst (24).

1.4   Spectral classifications of the Central Engine

The SINFONI spectra of the Central Engine (Figure 2, Table 3) show C III-IV and He II emission lines characteristic of a WC type WR star. The diagnostic C IV/C III $1.191/1.199\,\mu$m line ratio is close to 3.0, which matches that for WC7 stars (57) and is significantly greater than the 1.4 in the WC8 standard WR 135 (58), indicating the likely presence of a WC7 type star in the Central Engine of REX-1. The presence of a late-type WC star is also supported by the observed far-infrared colour excess in WISE, MSX (59), and IRAS (60) flux measurements of REX-1 (see Section 1.6).

However, the spectrum of REX-1 shows stronger He II and weaker C IV line emission than is stereotypical for a WC7 star. The emission line weakness is dilution by additional continuum, partly from dust emission, which increases with wavelength: e.g. the ratio of the He II $2.189/1.163$-μm lines is 0.16, compared with an average ~ 0.38 in other WC7 stars. The weakness in the J-band, where dust emission is negligible (top panel; Figure 2), points to the additional continuum from a companion star. The abnormal strength of the He II lines for a WC7 star suggests an early WN sub-type companion. The absence of N V and relative weakness of He I, and with comparison to WN spectra (61), implies the presence of a subtype WN4 or WN5 star. Such a double binary WR composition does require the ionisation type, temperature, and wind velocities of the two stars to be comparable if the lines are all formed in the same wind. Additionally, double WR binaries are rare, with very few known (e.g. (62)).

An alternative spectral subtype classification to the WC7+WN4-5 model, that equally well describes the spectra shown in Figure 2, is that of a WR star in the brief transitory phase between WN and WC (WN/WC) with an unseen OB-type companion. The WN/WC classification accurately describes the line ratios of the C III, C IV, and He I lines, and the abnormal strength of He II lines (20). However, WN/WC stars have never

been observed as dust producers, or as part of a Pinwheel nebula, despite several known binary systems (e.g. (63, 64)). One way to discern between a double WR binary or a WN/WC+O composition is through the detection of the $0.971\,\mu$m C III line. If system is a WN/WC+O, the $0.971\,\mu$m C III line would be relatively weak compared to the Helium lines, whereas the line would be strong for a double WR binary.

We favour the WC7+WN4-5 model for the Central Engine of REX-1, on the basis that no transitional WN/WC star has been observed to be a dust producer or part of a Pinwheel nebula, possibly on account of their low carbon abundances (65). In comparison, the prolific dust maker WR48a (e.g. (66)) appears to be a WC8+WN8h (67). In either event, spectroscopy of the Central Engine shows it to be a CWB, with at least one component a WR star. Independent of whether the binary is a double WR binary or a WN/WC+O, in both situations we would expect a wind an order of magnitude larger than that observed in the proper motion of the dust spiral seen in the VISIR data of REX-1.

1.5   Spectral properties of the distant Northern companion

The SINFONI spectra of the northern companion are presented in Figure 8. The near-infrared spectrum is dominanted by Paschen-β, Brackett-γ, and $1.083\,\mu$m He I (as shown by the IRIS2 data) line emission. In particular, the K-band spectrum resembles the O8Iaf supergiant HD151804 (68). However, the spectrum lacks the required $2.189\,\mu$m He II line of an O81af supergiant. Lacking any He II lines, the spectrum resembles the B1 Ia+ supergiant HD 169454 (69). However, that would imply a reasonably large high luminosity for a B1 Ia+ supergiant, with an absolute magnitude of -9.2. Despite this, we favour the northern companion being an B1 Ia+ supergiant but further observations, particularly optical spectra, are necessary to confirm this spectral type. We note that the $1.083\,\mu$m

He I and Paschen-β lines display a P-Cygni profile, both providing a measurement of a terminal windspeed of $\approx 900 \, \mathrm{km \, s^{-1}}$.

1.6 Optical and infrared photometry of REX-1

The SED derived from the infrared and optical photometry of REX-1 is provided in Figure 9. While our SINFONI and NACO data yield J-, K-band, 3.74- and 4.05-μm photometry of the Central Engine and Northern companion separately, all other data are for the system as a whole. Sources of the short wavelength photometry are the DECam Plane Survey (70) for g and r, the VPHAS+ survey (71) for r and i, the DENIS survey (72) for i (at a slightly longer wavelength, and treated separately for reddening and conversion to monochomatic fluxes), and the VVV survey (53) for Z. Infrared data for the system were taken from the 2MASS (73) survey for J, H and K_s, the AllWISE release from the WISE mission for $W1$, $W2$, $W3$, and $W4$, Spitzer GLIMPSE for the [5.8]-band, the AKARIIRC All-Sky (74) and FIS (75) surveys for $S9W$, $L18W$ and $N60$, the MSX SPIRIT III (76) for Bands A, C, D and E (8.28–21.3 μm), and the Herschel Hi-GAL survey (77) for the 70 μm flux.

Although the photometric data are heterogeneous in observation date and their coverage of the extended dust emission, we can use them for a robust measure of the interstellar reddening, the distance to the system, and to probe the dust formation history of REX-1.

The reddening was determined to be $A_V = 11.4$ by fitting the dust-free ($griZ$) photometry to the output flux of a WM-Basic (78) model for a 25 kK solar composition supergiant[1]. This model was selected for the Northern companion, which is assumed to dominate the SED at shorter wavelengths since it is 0.56 magnitude brighter in J-band, and brighter still at shorter wavelengths. For the interstellar reddening, we used the

---

[1]http://zuserver2.star.ucl.ac.uk/~ljs/starburst/BM_models/index.html

'Wd1+RCs' law (79), duly adjusted for the wavelengths of photometric bands used in the present study.

The REX-1 photometric data were observed over a long period, from 1996 (DENIS) to 2016 (DECam), and their reasonable consistency suggests that the stellar flux from REX-1 was not significantly variable over this interval. The J-band flux is seen to lie on the optically fitted SED (Figure 9), indicating that there is no significant contribution by dust emission at this wavelength.

It is evident that the form of the IR SED is quite unlike sterotypical dust making WR stars, which are generally Planckian, and which can be modelled using the smoothly varying carbon dust emissivity and Planck functions having temperatures T_g falling off with distance d from the stars as $T_g \propto d^{-0.4}$ (80). Instead, the REX-1 SED rises to peak near 12 μm, which is well defined by the MSX values. The MSX A and C–E bands have effective beam sizes of ≈ 21–$26''$, implying practically all of the flux from the extended dust cloud observed with VISIR should be captured by the MSX photometry. A simple model for the dust emission, an isothermal dust cloud fitted to the MSX data, yields T_g = 230 K and $1.2 \times 10^{-5} M_\odot$ of amorphous carbon grains (81). The flux from this model is plotted in Figure 9. The WISE $W4$, and Herschel Hi-GAL 70-μm fluxes are seen to consistent with it, suggesting that the mass of cool dust in this 'reservoir', and the stellar flux heating it, have not changed significantly since the MSX observations in 1996.

For more recent dust formation, we can also model the SED of the WR component using the fluxes from our SINFONI and NACO observations. We assume that there is no dust emission contribution in the J-band and model the WR wind flux with a power law of index -2.97 (82) and subtract this from the observations. The difference spectrum is fitted by an isothermal dust cloud having $T_g = 830$ K and mass $1.2 \times 10^{-8} M_\odot$ of carbon. This dust mass is in line with those determined for many WC7–9 stars (80) and almost

four orders of magnitude less than that in the extended cloud. Determination of the dust masses depends on the square of the distance to REX-1, here adopted to be 1.8 kpc, but their ratio does not. These results indicate that the dust formation rate of REX-1 has not been constant on a long (centuries) time-scale, but was significantly greater a $\sim$century ago, consistent with the CWB orbital derived from the plume's dynamical age.

1.7 X-ray properties of REX-1

The folded spectra for the X-ray observations of REX-1 are plotted in Figure 10. The spectra display the combination of heavy absorption with the features of a collisionally-ionised thermal plasma. For example, a strong emission line near 6.7 keV is present in all observations. We find the best fitting model is provided by a single photoelectrically absorbed optically-thin plasma model (apec), consistent with other known X-ray bright CWBs that all require winds with speeds $> 1000 \, \mathrm{km \, s^{-1}}$ to reproduce the required X-ray luminosities (83). During the fitting, the abundance parameter was allowed to vary. We do not get an improved fit for multi-temperature thermal plasma models, such as apec + apec. We also attempted to fit the spectra with a non-equilibrium collisionally ionised shock (vpshock) but got unrealistic shock ionisation ages. The best fitting parameters derived from the apec model for each observation are presented in Table 4.

The Fe Kα line profile does not change significantly between the observations, occurring at $6.69 \pm 0.01 \, \mathrm{keV}$. There are also statistically significant lines at 1.96 ± 0.04 and $2.44 \pm 0.03 \, \mathrm{keV}$ corresponding to Si Kα and S Kα.

As is evident by the different values of the observed 0.2 to 10 keV flux, $S_{\mathrm{x,obs}}$, REX-1 shows low long term ($> 1.5 \, \mathrm{year}$) X-ray variability. Such low long term variability, combined with the bright X-ray luminosity, is consistent with temperature of the collisional plasma changing in a CWB system with a period $\gtrsim 6$ months (84). A search for variability

30

internal to the XMM-Newton observations was also conducted. We performed a χ^2 and Rayleigh test (e.g. (42)) to identify any variability or a period signal within the range of 6.4 s to 12 h for the MOS1/MOS2 data, and 146 ms and 12 h for the pn data. We detected no significant variability and saw no significant power at any period. Additionally, the 2004 and 2008 XMM-Newton observations did not show time variability on timescales greater than 10 s according to a χ^2 test performed by the XMM-Newton pipeline (85). The lack of short-term variability makes the presence of a compact object in the system unlikely (84).

1.8   Radio properties of REX-1

From the ATCA measurements of REX-1, the flux density S was observed to increase from 27.9 ± 0.9 mJy at frequency ν of 19.7 GHz to 166 ± 15 mJy at 1.4 GHz. The radio spectrum is well described by a power-law with a spectral index of $\alpha = -0.71 \pm 0.05$, where $S \propto \nu^\alpha$. REX-1 was unresolved in all of the radio observations, with the highest resolution observation at 19.7 GHz having a synthesised beam profile of $0.74'' \times 0.29''$.

Such flux densities makes REX-1 the brightest non-thermal radio CWB discovered by over an order of magnitude, and the second brightest CWB detected in the radio outside of η Carinae (24). The relatively faint (< 20 mJy) radio flux densities of CWBs is usually explained by a combination of free-free absorption, lack of strong magnetic fields, and relatively weak shocks (24, 86). For REX-1 to be so bright in the radio, it is possible free-free absorption is significantly less than normal, which is consistent with asymmetric mass-loss model since the majority of potentially obscuring medium would be in a plane rotated to our line of sight to the shock region. Alternatively, a significantly stronger magnetic field (~ 20 kG) could be present in the system. Such a strong magnetic field is also predicted by rapid rotator models for WR stars (31).

REX-1 was also observed at 843 MHz by the Molonglo Observatory Synthesis Telescope (MOST) on six separate occasions between 1988 to 2006, mostly as part of the second epoch Molonglo Galactic Plane Survey-2 (MGPS-2) (87, 88). The flux densities of REX-1 in these images were calculated from MGPS-2 calibrated images and are presented in Figure 11. The lightcurve demonstrates that the REX-1 is variable at 843 MHz, with the flux density of REX-1 increasing from 85 mJy to 138 mJy between 1988 and 2006. The increase in the flux density appears to be linear with time, lending further evidence of a long-term secular evolution of the emission from REX-1, similar in time scale as implied by the wrapping of the dust spiral in the VISIR data. The type of linear variability displayed in Figure 11 also rules out refractive interstellar scintillation as the cause (89). The significant long term radio variability seems incongruent with the low X-ray variability. It is possible that the significant radio variability could be due to variation of the free-free absorption medium over the orbit (e.g. (90)), consistent with the model proposed in the main text of a greater than decade period orbit that takes the secondary star of the Central Engine through the dense equatorial plane populated by the slow, cool wind of the primary.

Table 1: Summary of the NACO observations of REX-1. Separation refers to the angular separation between the Central Engine and Northern companion, identified in the inset of Figure 1.

Wavelength (band) (μm)	Separation ($''$)	Central source magnitude	Outer source magnitude
2.24 (K)	0.739 ± 0.002	6.9 ± 0.2	8.1 ± 0.2
3.74 (L)	0.745 ± 0.008	4.7 ± 0.1	7.3 ± 0.1
4.05 (M)	0.75 ± 0.01	4.4 ± 0.3	7.0 ± 0.2

Table 2: Summary of the 0.2 and 10.0 keV observations of REX-1. ObsID corresponds to the unique identification number assigned to each observation by the respective X-ray observatory. T_{eff} is the total effective exposure time of the observation after filtering for background flaring.

Observatory	Epoch	ObsID	Off-axis angle ($'$)	Instrument	T_{eff} (s)
XMM-Newton	2004 Aug 10	0201500101	0.6	pn	8140
				MOS1	8480
				MOS2	8500
Chandra	2006 May 21	6687	8.6	ACIS-I3	49970
XMM-Newton	2008 Mar 20	0500300101	9.3	MOS1	51900
				MOS2	52870
XMM-Newton	2015 Mar 08	0742050101	8.8	pn	105600
				MOS2	136940

Table 3: Wavelengths (λ), identifications, and equivalent widths (EWs) of the lines identified in the SINFONI and IRIS2 spectra of the Central Engine. EWs of blends are given for the first contributor only, with others marked '(bl)'.

λ (μm)	Line ID	EW (Ang.)
1.083	He I 2p-2s	87
1.163	He II (7-5)	156
1.191	C IV (8-7)	59
1.199	C III 4p-4s	19
1.256	C III (9-7)	17
1.282	He I (5-3)	56
1.282	He II (10-6)	(bl)
1.476	He II (9-6)	36
1.476	C IV (18-12)	(bl)
1.552	O V (10-9)	4
1.572	He II (13-7)	36
1.575	C III (13-9)	(bl)
1.693	He II (12-7)	29
1.701	He I 4d-3p	(bl)
1.736	C IV (9-8)	31
2.078	C IV 3d-3p	43
2.108	C III 5p-5s	26
2.113	He I 4s-3p	(bl)
2.117	C III (8-7)	(bl)
2.189	He II (10-7)	25

Table 4: The best-fit parameters of the `apec` model to the X-ray observations of REX-1. All reported errors are for 90% confidence. The abundances are relative to solar abundances (91). $S_{x,obs}$ and $S_{x,unabs}$ are the observed and unabsorbed 0.2 to 10.0 keV flux, respectively.

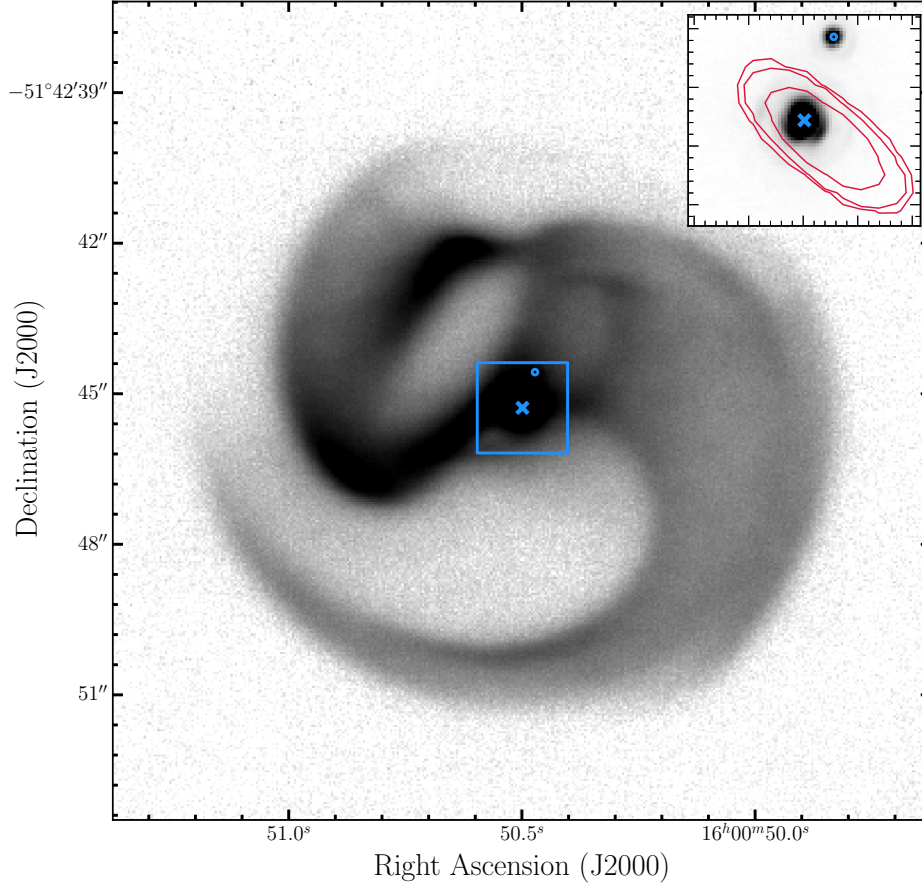| Epoch	kT (keV)	$N_{\rm H}$ (10^{22} cm^{-2})	Abundances	$S_{x,obs}$ $S_{x,unabs}$ (10^{-12} ergs cm^{-2} s^{-1})		χ^2/dof ($\chi^2_{\rm red}$)
2004 Aug 10	5.6 ± 0.5	2.8 ± 0.1	0.5 ± 0.1	9.2 ± 0.2	17.8 ± 0.6	551/510 (1.08)
2006 May 21	4.6 ± 0.3	3.10 ± 0.08	0.7 ± 0.1	8.4 ± 0.2	17.1 ± 0.4	392/352 (1.11)
2008 Mar 20	6.3 ± 0.4	2.7 ± 0.1	0.8 ± 0.1	9.6 ± 0.2	17.6 ± 0.3	821/677 (1.21)
2015 Mar 08	5.1 ± 0.2	2.76 ± 0.05	0.48 ± 0.04	8.1 ± 0.1	16.3 ± 0.2	1214/858 (1.42)

Figure 1: VISIR $8.9\,\mu m$ image of REX-1 taken on 13 August 2016, displaying the exotic dust pattern being sculpted by the system. The $2.24\,\mu m$ NACO image of the region bounded by the blue box, of dimenson $1.8'' \times 1.8''$, is shown in the upper right corner. The position of the Central Engine and the Northern companion identified in the NACO image are indicated by the blue cross and circle, respectively. The over-plotted red contours are from our $19.7\,\mathrm{GHz}$ ATCA observation, with contour levels correponding to 5, 10 and 50 times the rms noise $(8 \times 10^{-2}\,\mathrm{mJy\,beam}^{-1})$. The dimensions of the ATCA synthesised beam are $0.74'' \times 0.29''$, with a position angle of $50.1°$. The stretch on the VISIR image is chosen to accentuate the dust pattern, with 80% of the flux of the VISIR image coming from the area bounded by the blue box.
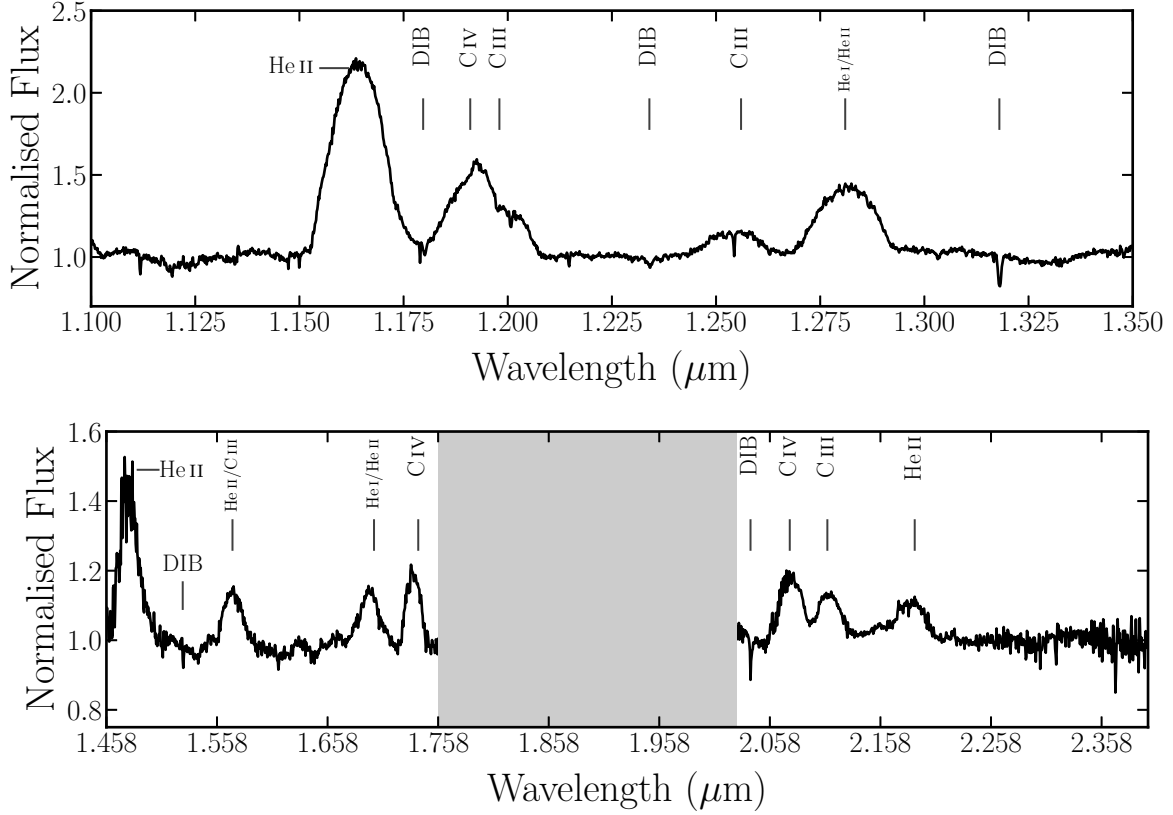
Figure 2: SINFONI *J*-band (top) and *H*+*K*-band (bottom) spectra for the Central Engine at the centre of NACO image shown in the inset of Figure 1. Prominent emission lines are labelled and the wavelength range where telluric correction was not possible between the *H*- and *K*-bands is indicated in gray. Known and suggested diffuse interstellar absorption bands are labelled by 'DIB', with the DIB line indicated at $2.02\,\mu$m likely the first DIB detected in *K*-band.
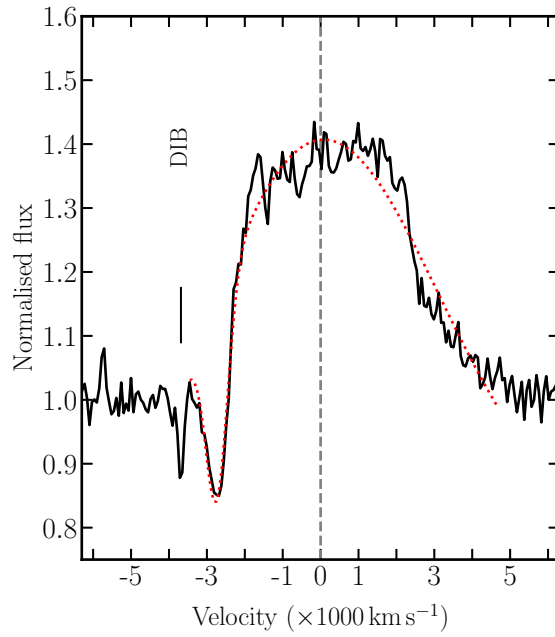
Figure 3: $1.083\,\mu\mathrm{m}$ He I line from the continuum-corrected IRIS2 long-slit J_s-band spectrum of REX-1. The known diffuse interstellar band is identified by the label 'DIB'. The fit to the P-Cygni profile is shown by the red-dashed curve, providing a measurement of a terminal velocity $v_\infty = 3400 \pm 200\,\mathrm{km\,s^{-1}}$.
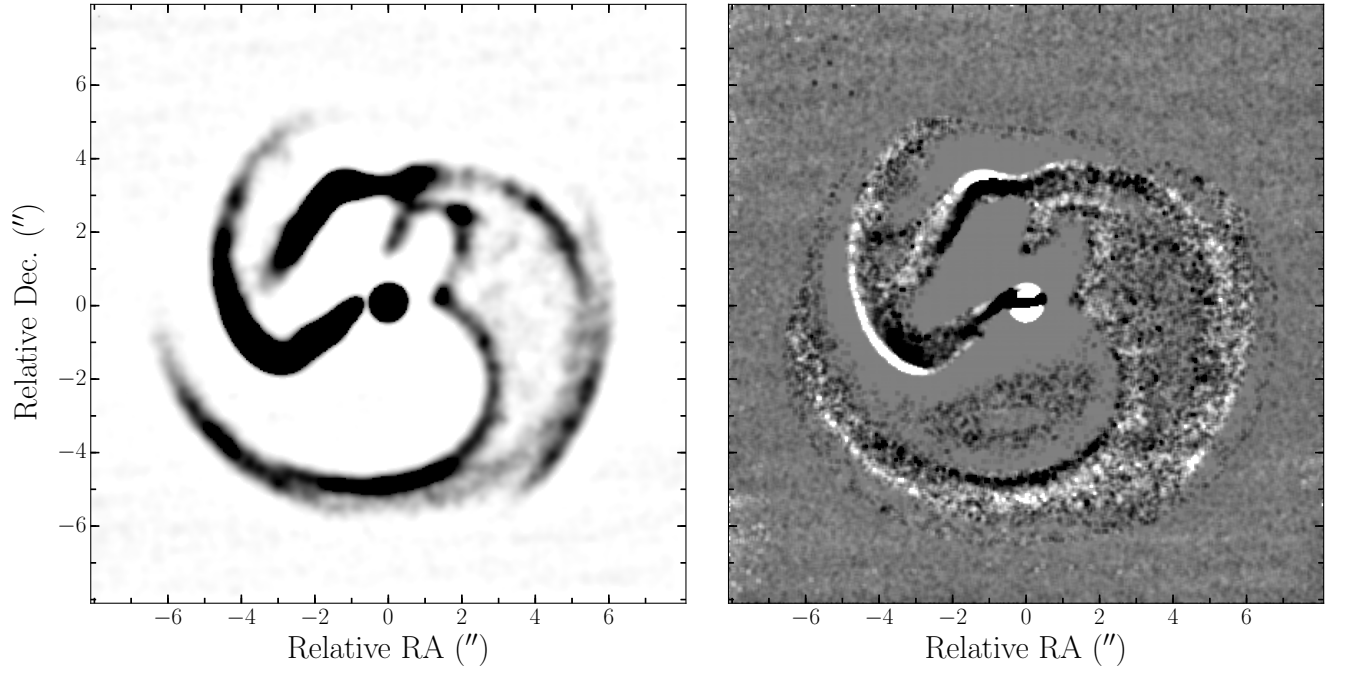
Figure 4: Left Panel: a highpass filtered image of the 1 August 2017 $8.9\,\mu$m image of REX-1, centered on the position of REX-1, which emphasizes the location of edges and boundaries of the plume structure. Right Panel: an illustration of the proper motion recorded over the ~year interval between the two VISIR epochs is provided by subtracting the 2016 from the 2017 highpass filtered images, also centered on the position of REX-1. The real displacement in the edges and boundaries demarking the dust over the interval is witnessed as the newer epoch (white) is found exterior to the older epoch (black).
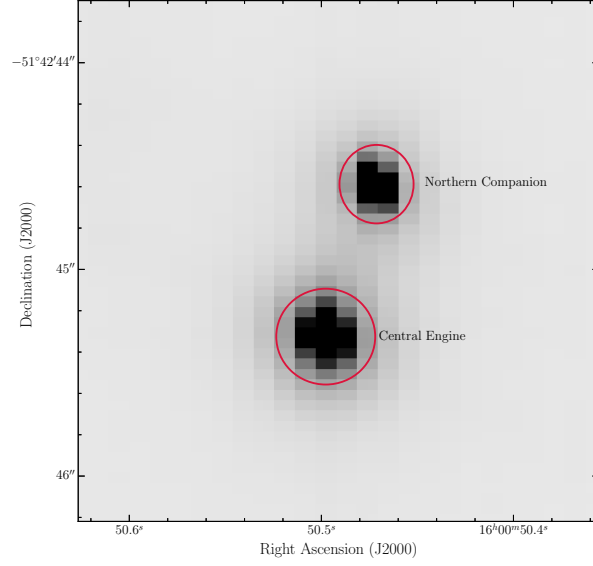
Figure 5: SINFONI $H+K$-band image of REX-1, with the spectral extraction regions shown by the red ellipses. Similar to the NACO images of REX-1, SINFONI resolves REX-1 into two components, a Central Engine and a Northern companion.
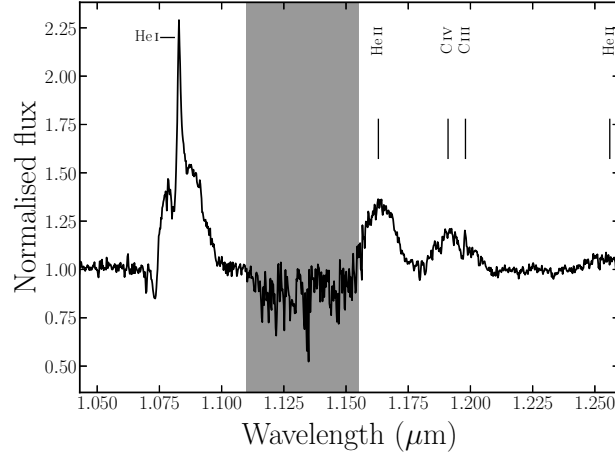

Figure 6: Continuum-corrected long-slit J_s-band IRIS2 spectrum of REX-1 for the full $1''$ aperture (implying the spectrum is the superposition of the Central Engine and Northern companion), with the detected emission lines indicated. The noise in the spectrum is higher between 1.11 and $1.155\,\mu m$, indicated by grey shading, due to imperfect telluric correction in that wavelength range.
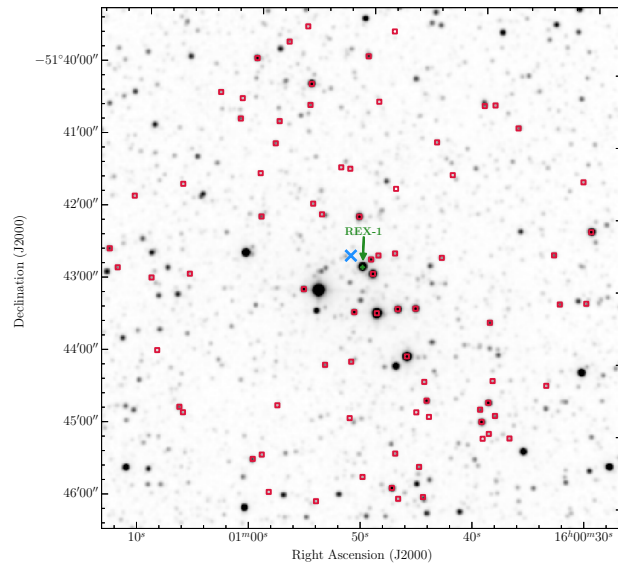
39

Figure 7: 2MASS *J*-band image of the young open cluster Majaess 170, with the cluster members marked by red squares (51). The blue cross represents the centre of the cluster (47). The position of REX-1 is indicated by the green arrow and addition sign.
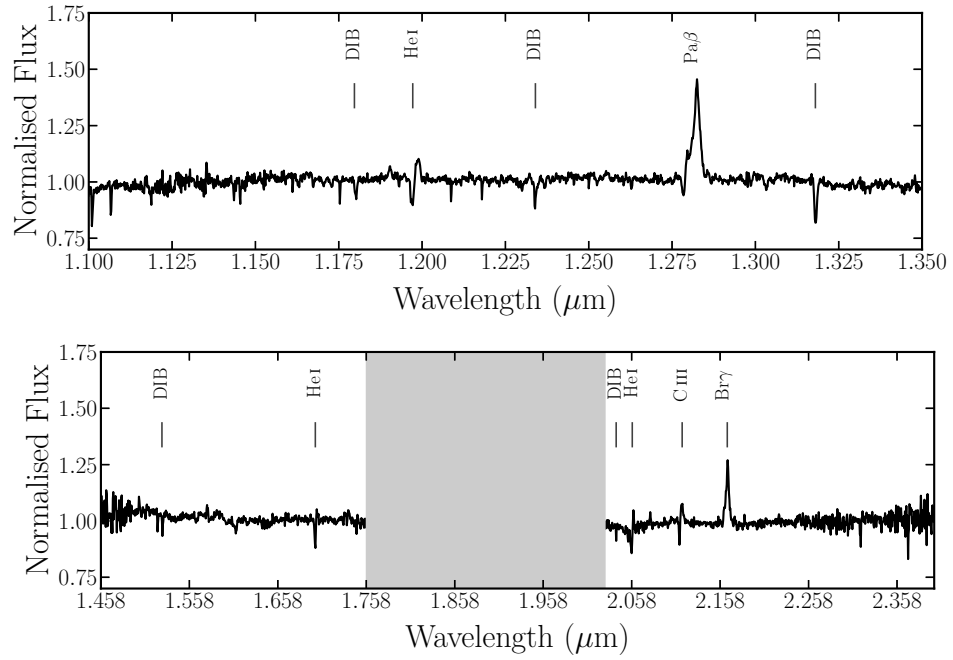
Figure 8: SINFONI *J*-band (top) and *H+K*-band (bottom) spectra for the Northern companion. Prominent emission lines are labelled and the area where telluric correction was not possible in the *H+K*-band is indicated in gray. Known and suggested diffuse interstellar bands are labelled by 'DIB'.
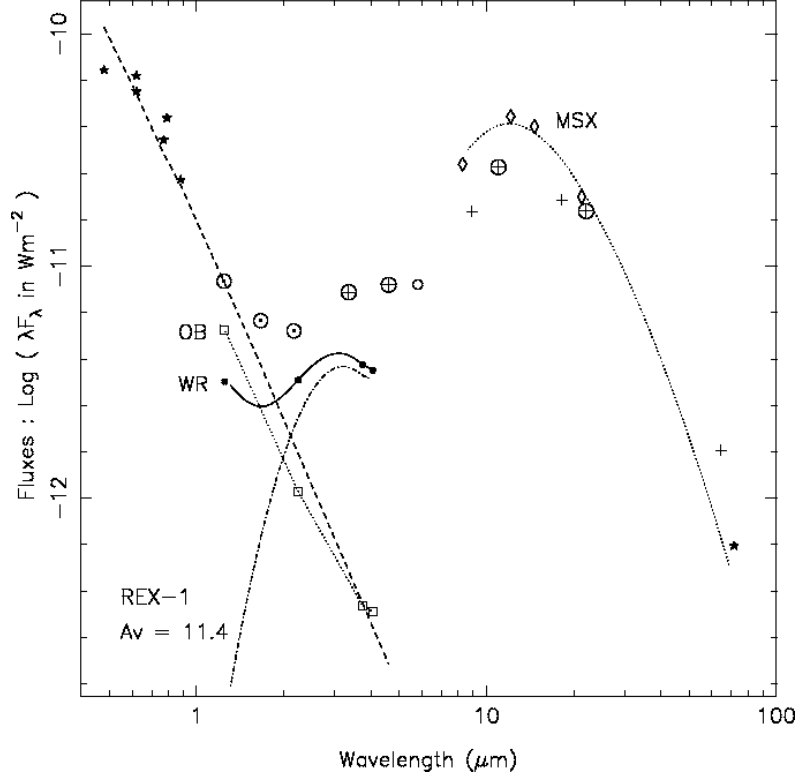
Figure 9: De-reddened optical to far-infrared SED of REX-1. Fluxes were computed from g, r, i and Z from the DECam Plane (marked $\star$), VPHAS+, DENIS and VVV surveys, J-, H- and K_s-band from 2MASS (marked $\odot$), $W1$, $W2$, $W3$, and $W3$ from WISE (marked $\oplus$), [5.8]-band from GLIMPSE (marked $\circ$), $S9W$, $L18W$, $N60$ and $WIDE - S$ from AKARI (marked $+$), MSX A, C, D and E (marked $\Diamond$) and the 70-micron Hi-GAL flux (marked $\star$). The dashed line fitted to the $g - Z$ points represents the SED of a $25\,\mathrm{kK}$ supergiant, adopted for the Northern companion and assumed to dominate the SED at these shorter wavelengths. Fluxes for the individual Central Engine and Northern companion measured from our SINFONI and NACO observations are plotted $\bullet$ ('WR') and $\square$ ('OB'), respectively. The latter, joined by a dotted line, are consistent with a stellar continuum, while the former (joined by a solid line) are modelled with the sum of a WR wind continuum fitted to J-band plus heated dust; the SED of that dust is also plotted dash-dot.
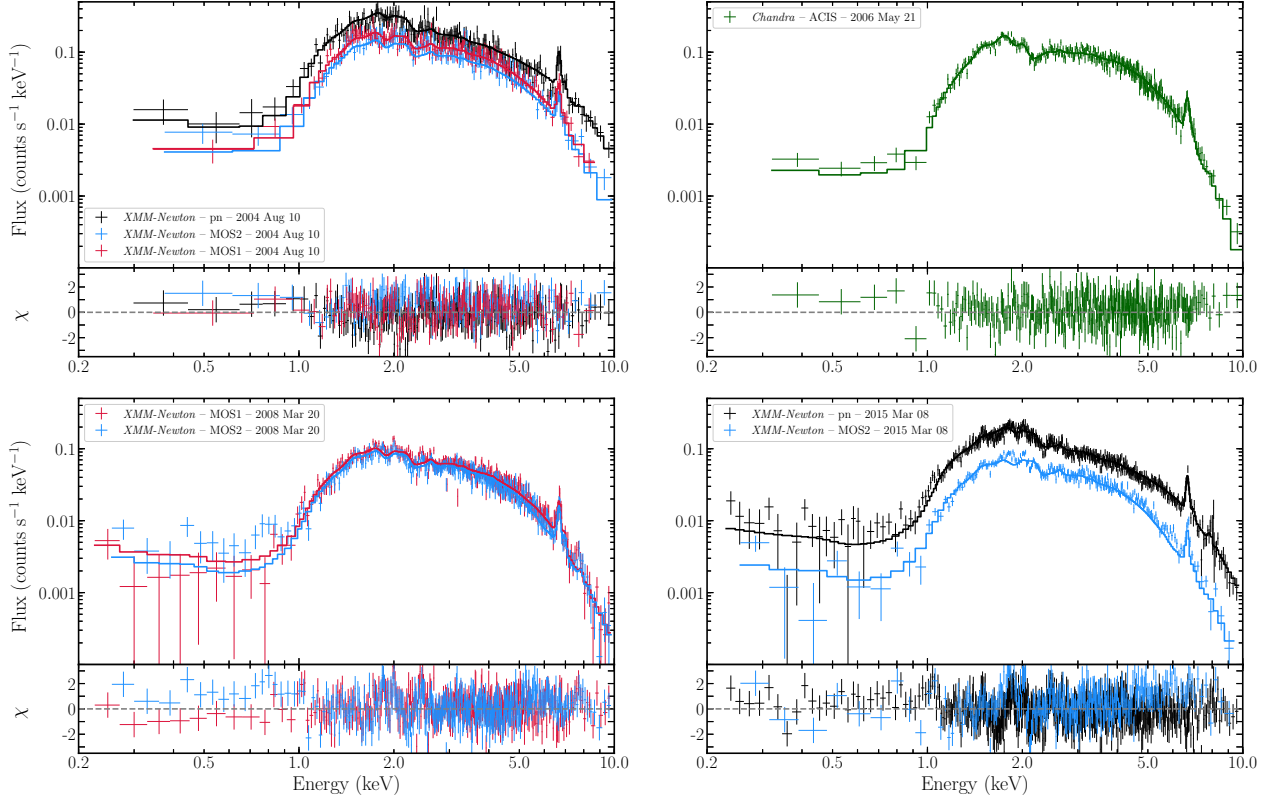
42

Figure 10: The folded X-ray spectra observed by XMM-Newton and Chandra with the best fit thermal plasma `apec` model over-plotted, using the parameters listed in Table 4. The legend in each panel reports the observing X-ray telescope, X-ray instrument, and the epoch of the observation. The χ-values for the model fits are displayed below the spectrum for each epoch, and are coloured corresponding to the X-ray instrument. pn, MOS1, MOS2, and ACIS are coloured black, red, blue, and green, respectively.
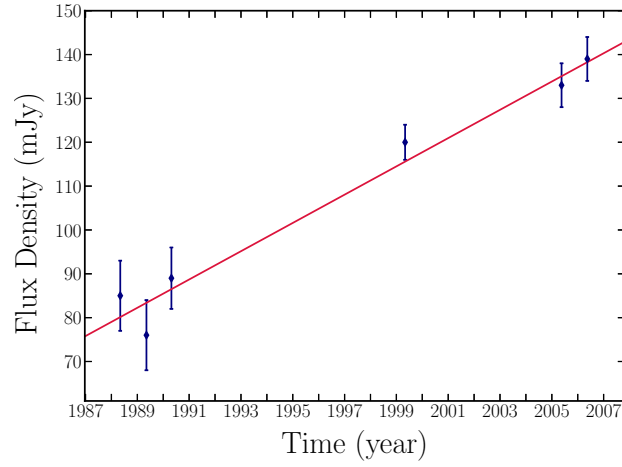
Figure 11: 843 MHz radio lightcurve of REX-1 between 1988 and 2006. The red line is the best fit to the data, and predicts a flux density of 175 ± 15 mJy for May 2017, when the targeted ATCA observations were performed. The gradient of the line implies the source brightens $3.2 \, \mathrm{mJy \, yr^{-1}}$ at 843 MHz.